Advanced PHOTONICS

Tailoring light on three-dimensional photonic chips: a platform for versatile OAM mode optical interconnects

Jue Wang,[a,b,†] **Chengkun Cai,**[a,b,†] **Feng Cui,**[a,b] **Min Yang,**[a,b] **Yize Liang,**[a,b] **and Jian Wang**[a,b,*]

[a]Huazhong University of Science and Technology, Wuhan National Laboratory for Optoelectronics and School of Optical and Electronic Information, Wuhan, China

[b]Optics Valley Laboratory, Wuhan, China

Abstract. Explosive growth in demand for data traffic has prompted exploration of the spatial dimension of light waves, which provides a degree of freedom to expand data transmission capacity. Various techniques based on bulky optical devices have been proposed to tailor light waves in the spatial dimension. However, their inherent large size, extra loss, and precise alignment requirements make these techniques relatively difficult to implement in a compact and flexible way. In contrast, three-dimensional (3D) photonic chips with compact size and low loss provide a promising miniaturized candidate for tailoring light in the spatial dimension. Significantly, they are attractive for chip-assisted short-distance spatial mode optical interconnects that are challenging to bulky optics. Here, we propose and fabricate femtosecond laser-inscribed 3D photonic chips to tailor orbital angular momentum (OAM) modes in the spatial dimension. Various functions on the platform of 3D photonic chips are experimentally demonstrated, including the generation, (de)multiplexing, and exchange of OAM modes. Moreover, chip-chip and chip–fiber–chip short-distance optical interconnects using OAM modes are demonstrated in the experiment with favorable performance. This work paves the way to flexibly tailor light waves on 3D photonic chips and offers a compact solution for versatile optical interconnects and other emerging applications with spatial modes.

Keywords: orbital angular momentum; three-dimensional photonic chips; femtosecond laser writing; spatial modes; chip–chip; chip–fiber–chip; optical interconnects.

Received Feb. 3, 2023; revised manuscript received Mar. 27, 2023; accepted for publication Apr. 13, 2023; published online May 24, 2023.

1 Introduction

Increasing data transmission capacity is a persistent demand for optical interconnects. Recently, different physical dimensions of light waves, including time,[1] amplitude,[2] phase,[3] wavelength,[4] and polarization,[5] have been fully utilized to scale the data traffic. Even though various multiplexing techniques exploiting these physical dimensions have been developed, it is becoming rather difficult to follow the demand of a global network that is growing by 40% annually.[6] To keep pace with the ever-increasing demand, a new physical dimension of light is urgently needed. Fortunately, space-division multiplexing technology that transmits orthogonal spatial modes loaded with different signals in an optical interconnect system has further improved the transmission capacity, providing a new degree of freedom for capacity scaling of optical interconnects[7–9] [Fig. 1(a)]. The utilization of the spatial modes in optical interconnects systems requires the development of key optical devices, including spatial mode generators, (de)multiplexers, and exchangers. Traditional optical devices manipulating the spatial modes rely on bulky optics, such as phase plates[10,11] or spatial light modulators,[12,13] which take up too much space and are unscalable. To meet the requirement of a compact solution, the miniaturization of these key optical devices is of great importance.

*Address all correspondence to Jian Wang, jwang@hust.edu.cn

†These authors contributed equally to this work.
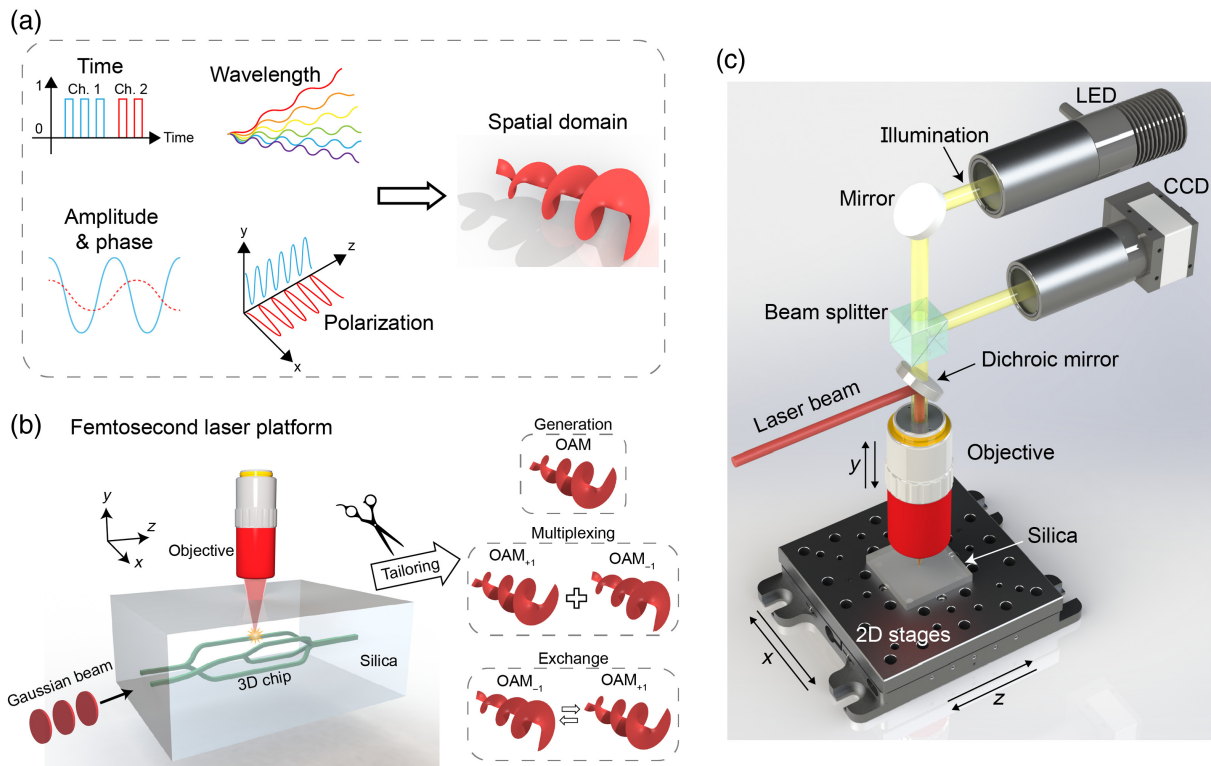
Fig. 1 (a) Multiple physical dimensions of light waves: from traditional ones to the spatial domain (e.g., OAM modes). (b) Concept of 3D photonic chips fabricated by FSLW for tailoring spatial modes (OAM generation/multiplexing/exchange). (c) Fabrication setup for FSLW.

Integrated photonic chips with a small footprint, high efficiency, and low cost are emerging with the rapid development of silicon photonics. Remarkably, most optical devices based on silicon photonics, including lasers,[14–16] modulators,[17,18] switches,[19,20] filters,[21,22] and (de)multiplexers,[23,24] have been widely implemented. Moreover, to further increase the density of integration, three-dimensional (3D) photonic chips have also been demonstrated with the advent of multilayer photonic structures.[25,26] However, these state-of-the-art integration technologies are typically implemented in a modified complementary-metal-oxide-semiconductor process, with the disadvantages of inflexibility and complex process. Thus, flexible fabrication of 3D photonic chips is still a challenge. Fortunately, femtosecond laser writing (FSLW) has been an emerging technique capable of fabricating 3D structures with microscale resolution. The FSLW induces a localized change of the refractive index near the laser foci in the silica substrate (see Appendix). By designing the 3D trajectory of the foci, we can create various photonic devices. Several 3D photonic integrated devices have been demonstrated using the FSLW, such as splitters,[27] mode selective couplers,[28] photonic lanterns,[29–31] and space-division multiplexers.[32–35]

In this work, we propose and demonstrate FSLW-based 3D photonic chips for orbital angular momentum (OAM) mode-[36–40] enabled optical interconnects. Two kinds of 3D photonic chips based on the trench waveguides are designed and fabricated to tailor the spatial modes, realizing the generation, multiplexing, demultiplexing, and exchange of OAM modes [Fig. 1(b)]. We use the setup illustrated in Fig. 1(c) for FSLW to fabricate these 3D photonic chips. We also deploy the fabricated 3D photonic chips in mode-division multiplexing (MDM) systems,

characterizing their performance in chip-chip and chip–fiber–chip optical interconnects.

2 Results

2.1 On-Chip OAM Mode Generation

In this work, the first 3D photonic chip for spatial mode tailoring is an on-chip OAM mode generator; its concept and principle are illustrated in Fig. 2(a). The chip is fabricated using the FSLW technique. The detailed fabrication process can be seen in the Appendix. The on-chip OAM mode generator consists of an input waveguide, a Mach–Zehnder interferometer (MZI), and a trench waveguide. The input waveguide and the trench waveguide are designed to support the fundamental and higher-order modes. The principle of the on-chip OAM mode generator is as follows. First, the light launched into the input waveguide excites the fundamental mode. Then the MZI structure (colored by red) that introduces a phase shift in one arm converts the fundamental mode to the first-order quasi-transverse electric mode (TE_{10}) (see Note 1 in the Supplementary Material). The generation of the OAM mode is based on the specially designed trench waveguide. The TE_{10} mode can be considered as the in-phase combination of the diagonally and anti-diagonally distributed linearly polarized (LP)-like modes. When the phase difference between these two LP-like modes is $\pi/2$ or $-\pi/2$, the OAM mode with a topological charge of -1 or $+1$ is generated.

The trench waveguide and its supported eigenmodes are shown in Fig. 2(b). Four parameters define the geometry, which are the waveguide width (W_1), waveguide height (H_1), trench width (w_1), and trench height (h_1). The trench waveguide
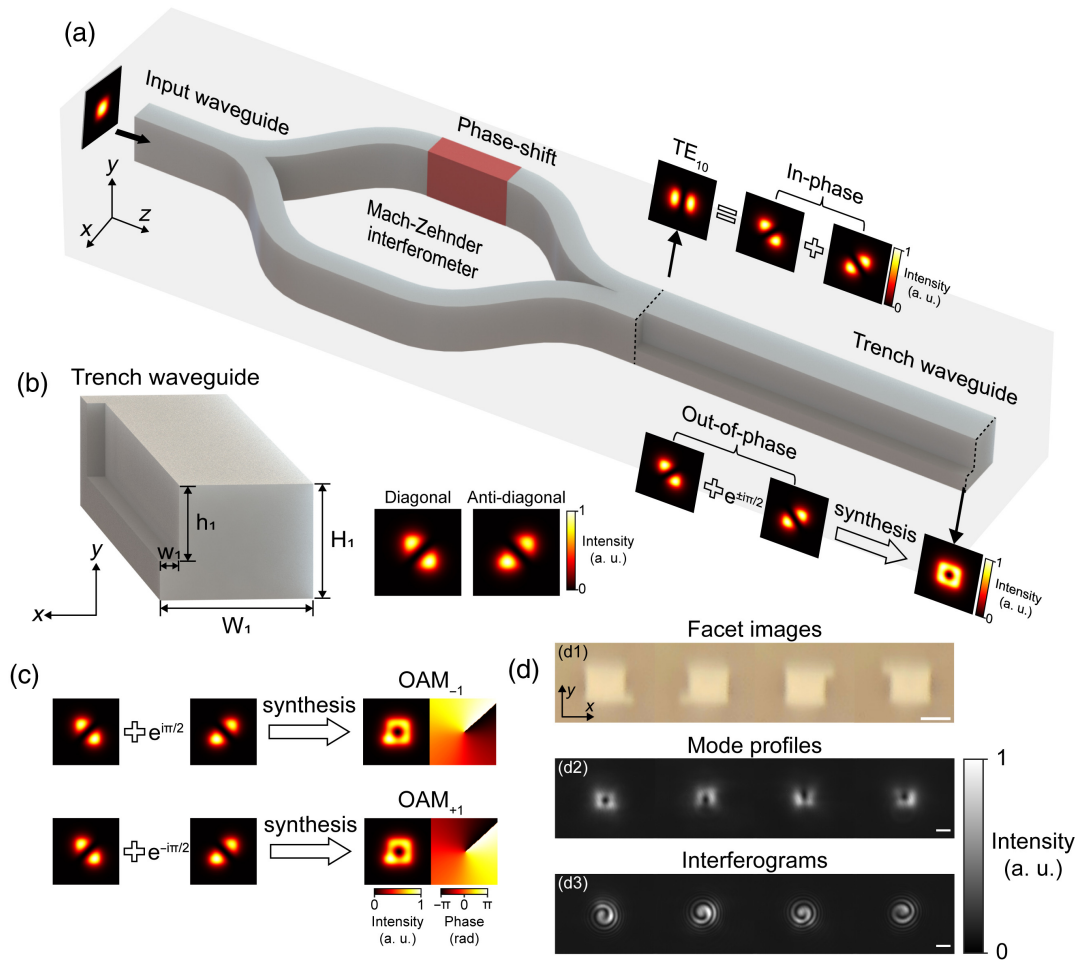
Fig. 2 On-chip OAM mode generator. (a) Concept and principle of the trench-based OAM generator. (b) Structure of trench waveguide and its supporting higher-order modes. (c) Simulated LP-like modes and their synthesized OAM modes. (d) Experimental results of OAM generator with different trench locations: (d1) trench facet images captured by an optical microscope, (d2) measured mode profiles, and (d3) measured interferograms (interference with a reference Gaussian beam). Scale bar, 20 μm.

supports two orthogonal LP-like modes at 1550 nm, which are diagonally and antidiagonally distributed by choosing the proper geometry (see Note 2 in the Supplementary Material). Here, the W_1 and H_1 are set to 17 and 15 μm, respectively. w_1 and h_2 are set to 3 and 9 μm, respectively. These two LP-like modes are nondegenerate due to the asymmetrical structure. Thus, the TE_{10} mode can simultaneously excite two orthogonal LP-like modes with different propagation constants. Further, as depicted in Fig. 2(c), they can be synthesized to OAM modes with topological charges of -1 and $+1$ after propagating through different distances, corresponding to phase differences of $\pi/2$ and $-\pi/2$, respectively. Except for changing the length of the trench waveguide, one can also swap the sign of the topological charge of OAM modes by altering the trench location.

The experimental results for the OAM generation with different trench locations are shown in Fig. 2(d), where (d1) $\sim$ (d3) are the facet images of the trench waveguides, output mode profiles, and corresponding interferograms (by interference with a reference Gaussian beam), respectively. These four OAM

generators are entirely the same, except for the location of the trench structure. We characterize these OAM modes by retrieving their phase profiles and calculating their OAM spectra (see Note 3 in the Supplementary Material). The OAM phase purities for each case are >92%. The details of phase retrieving and mode purity calculation can be found in the Appendix. The measured mode profiles in Fig. 2(d2) show slight defects in the experiment, which are mainly caused by the slight fabrication error of waveguide structures, i.e. inaccurate phase difference (derivation from π) between the two arms of the MZI as well as inaccurate phase difference (derivation from $\pm\pi/2$) between the two eigenmodes of the trench waveguide. However, they still show a high OAM phase purity over 92%. The mode quality might be improved by further reducing the fabrication error with optimized fabrication parameters, such as the laser power, scanning speed, and scanning spacing.

In the experiment, when the polarization state of the input beam changes, the output OAM mode profile keeps almost unchanged, and the polarization state of the output OAM mode almost remains the same as the input beam. That is
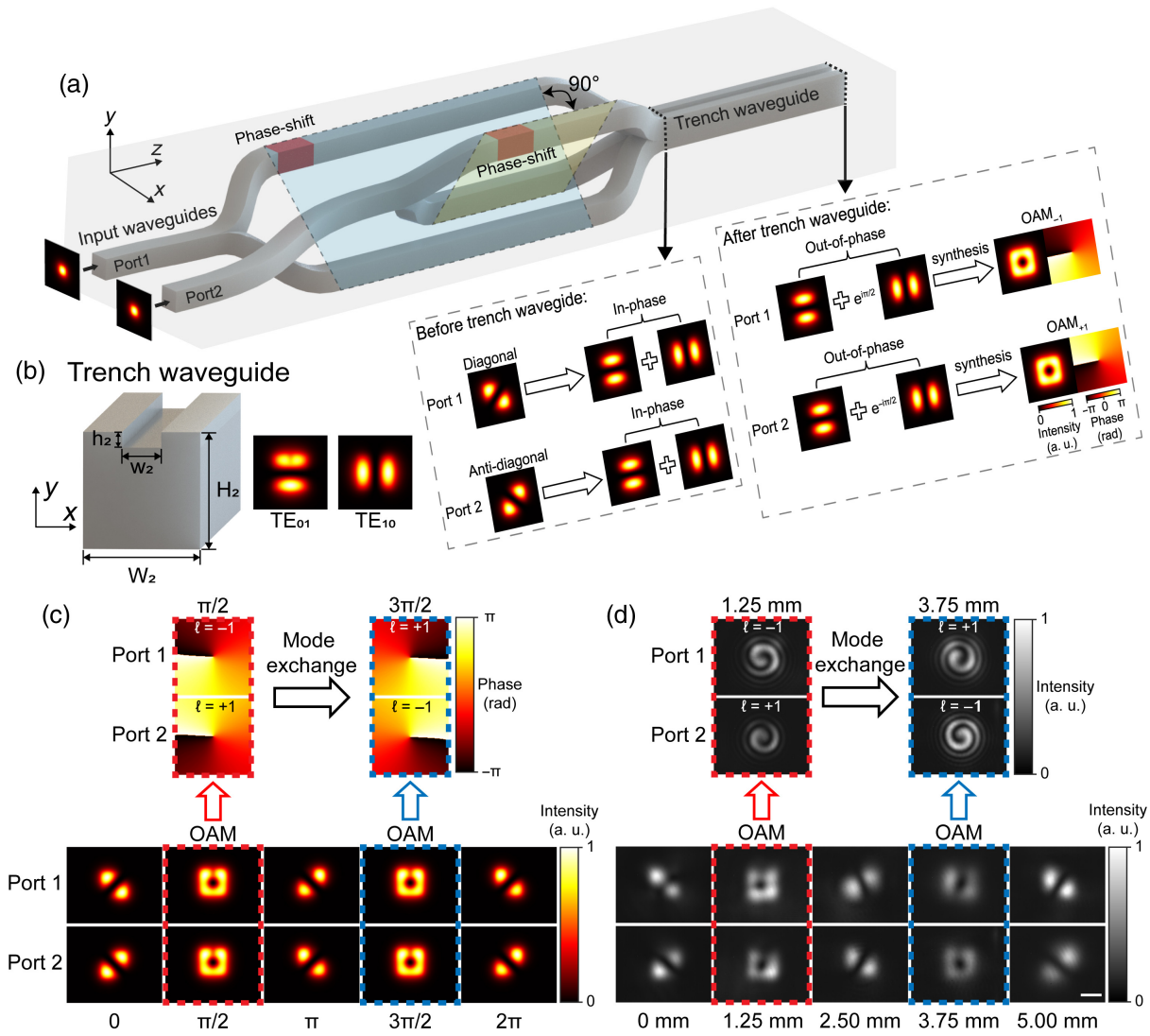
Fig. 3 On-chip OAM mode multiplexer. (a) Concept and principle of the trench-based OAM mode multiplexer. (b) Structure of the trench waveguide and the supported higher-order eigenmodes (TE$_{01}$ and TE$_{10}$). (c) Simulation results of OAM mode multiplexer and exchanger. (d) Experimental results of OAM mode multiplexer and exchanger. Scale bar, 20 μm.

because, according to our characterization in the experiment, the birefringence induced by FSLW is estimated to be lower than 1×10^{-5}. Meanwhile, the waveguide structures of the 3D photonic chip are relatively symmetrical and short in length.

2.2 On-Chip OAM Mode (De)Multiplexer and Exchanger

Other typical functions for spatial mode tailoring are mode (de)multiplexing and exchange. We propose an on-chip OAM mode multiplexer based on the variation of the trench waveguide; its concept and principle are illustrated in Fig. 3(a). The OAM mode multiplexer consists of two input waveguides, two MZIs, and a specially designed trench waveguide. The angle between the planes (colored cyan and yellow) where the two MZIs are located is 90 deg. At port 1, the fundamental mode is converted to an LP-like mode with the diagonal distribution by

the MZI. Before the trench waveguide, the LP-like mode excites two higher-order TE$_{01}$ and TE$_{10}$ modes equal in phase. Then when the phase difference of these two modes is $\pi/2$, the OAM mode with the topological charge of -1 is generated at the output. The same principle is applied to port 2, except for the opposite sign of phase difference ($-\pi/2$) and topological charge number ($+1$) of the OAM mode.

Figure 3(b) shows the detailed structure of the trench waveguide and the higher-order eigenmodes (TE$_{01}$ and TE$_{10}$) that the waveguide supports. Unlike the former, the trench here is located at the middle top of the waveguide rather than the corners. W_2 and H_2 are the waveguide width and height, respectively. w_2 and h_2 are the trench width and height, respectively. By introducing a small trench structure, the degeneracy of TE$_{01}$ and TE$_{10}$ modes is lifted, which means they have different effective refractive indices. The length of the trench waveguide L can be expressed by

$$L = \frac{\lambda \Delta\varphi}{2\pi \Delta n_{\text{eff}}}, \qquad (1)$$

where $\Delta\varphi$ and Δn_{eff} are the phase difference and effective refractive index difference between the two eigenmodes (TE_{01} and TE_{10}), and λ is the wavelength in vacuum. When the trench becomes large, the effective refractive index difference Δn_{eff} between the two eigenmodes also increases [see Fig. S4(b) in the Supplementary Material]. So, according to Eq. (1), a larger Δn_{eff} results in a shorter L for $\Delta\varphi = \pm\pi/2$ (e.g. required phase difference for the synthesis of OAM modes). However, the increasing trench size may degrade the uniformity of the TE_{01} mode, resulting in the reduced mode purity of the output OAM mode [see Fig. S4(a) in the Supplementary Material]. Therefore, an optimized trench size should be considered to achieve high mode quality with a relatively short device. Once the optimized size of the trench structure is chosen, the Δn_{eff} is determined. Thus we can produce OAM modes by propagating through a proper length of the trench waveguide with the accumulated phase difference of $\Delta\varphi = \pm\pi/2$. The detailed analyses on how to balance the length of the trench waveguide and output mode quality can be seen in Note 4 in the Supplementary Material.

Simulation results of the OAM mode multiplexer for input from ports 1 and 2 with phase differences of 0, $\pi/2$, π, $3\pi/2$, and 2π between TE_{01} and TE_{10} modes in the trench waveguide are depicted in Fig. 3(c). When the phase difference is 0 (π), the outputs are diagonally and anti-diagonally (anti-diagonally and diagonally) distributed LP-like modes for input from ports 1 and 2. When the phase difference is $\pi/2$ ($3\pi/2$), the outputs are OAM modes with the topological charge of -1 and $+1$ ($+1$ and -1) for input from ports 1 and 2, verified by their phase profiles. Also, it can be seen that the mode exchange happens when the phase difference changes from $\pi/2$ to $3\pi/2$.

We experimentally demonstrate the OAM mode multiplexing and exchange in our fabricated 3D photonic chip. Figure 3(d) shows a similar mode evolution with our simulation results in Fig. 3(c). When the trench length is 0 or 5.00 mm, corresponding to the phase difference of 0 or 2π, the mode profiles are diagonally and anti-diagonally distributed LP-like modes for input from ports 1 and 2. When the trench length is 2.50 mm, corresponding to the phase difference of π, the mode profiles rotate 90 deg for input from ports 1 and 2, which are anti-diagonally and diagonally distributed LP-like modes. The OAM mode multiplexing happens when the trench length is 1.25 mm. OAM_{-1} and OAM_{+1} modes are generated under this condition; this is verified by their interferograms. By extending the trench length to 3.75 mm, OAM modes swap with each other, where OAM_{-1} is converted to OAM_{+1} for input from port 1, and OAM_{+1} is converted to OAM_{-1} for input from port 2 simultaneously.

Furthermore, we characterize all four OAM modes, retrieving their phase profiles and calculating their OAM spectra (see Note 5 in the Supplementary Material). The OAM phase purities are $>92\%$. The details of phase retrieving and mode purity calculation can be found in the Appendix. Similar to the OAM mode multiplexer, we can also realize the OAM mode demultiplexer simply by using it in an opposite way.
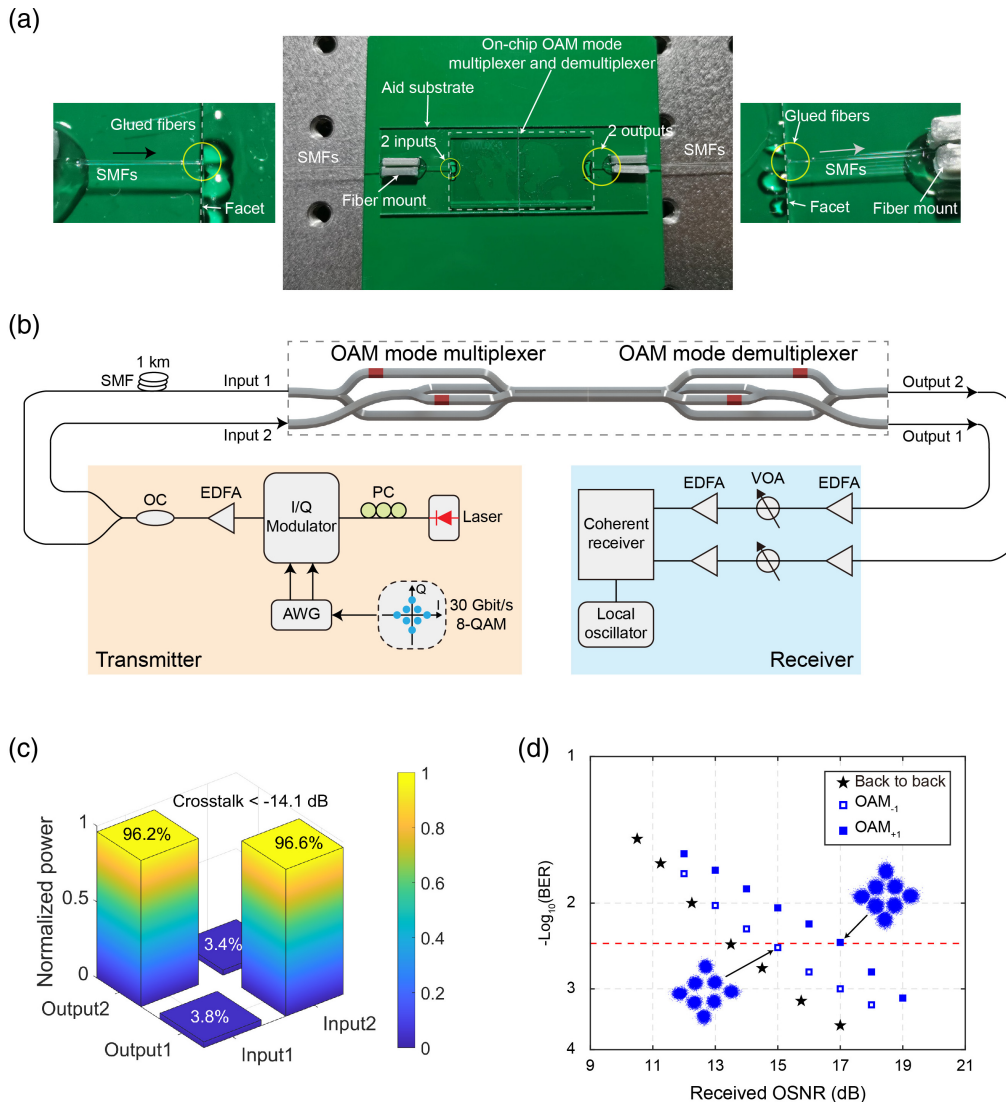
2.3 Chip–Chip Optical Interconnects

Using the designed and fabricated 3D photonic chips for MDM with OAM modes, we demonstrate the chip–chip optical

interconnects. The fabricated 3D photonic chips are packaged with single-mode fibers (SMFs) first, as shown in Fig. 4(a). The detailed packaging procedure can be found in Note 6 in the Supplementary Material. The experimental setup for chip–chip optical interconnects is shown in Fig. 4(b). A 1550-nm laser is modulated by an optical I/Q modulator driven by an arbitrary waveform generator (AWG) to generate the 30 Gbit/s 8-ary quadrature amplitude modulation (8-QAM) signal at the transmitter side. A polarization controller (PC) is used to optimize the state of polarization. The amplified optical signal by an erbium-doped fiber amplifier (EDFA) is divided into two channels by an optical coupler (OC), and one of them is transmitted through an additional 1-km SMF for decoherence. Two channel optical signals carried by Gaussian modes are first coupled into an OAM mode multiplexer from inputs 1 and 2, which are transformed into OAM_{-1} and OAM_{+1} modes through the 1.25-mm trench waveguide. These two OAM modes are then coupled into an OAM mode demultiplexer with a trench of the same length and are converted back to Gaussian modes at outputs 1 and 2. The output optical signals are amplified by another EDFA on the receiver side. Then a coherent receiver followed by a local oscillator is used to analyze 8-QAM signals for the performance evaluation. Variable optical attenuators (VOAs) and the following EDFAs are used to adjust the received optical signal-to-noise ratio (OSNR). The measured crosstalk matrix for two inputs and two outputs is plotted in Fig. 4(c), which is < -14.1 dB. The measured bit-error rate (BER) curves for OAM modes transmission are plotted in Fig. 4(d). Compared to the back-to-back case, the measured OSNR penalties at a BER of 3.8×10^{-3} [7% overhead hard-decision forward-error correction (HD-FEC) threshold] for multiplexing transmission of OAM_{-1} and OAM_{+1} modes are less than 1.3 and 3.5 dB, respectively. The insets in Fig. 4(d) are their typical constellations.

2.4 Chip–Fiber–Chip Optical Interconnects

Using the designed and fabricated 3D photonic chips for MDM with OAM modes, we also demonstrate the chip–fiber–chip optical interconnects. Here, we use two individual OAM modes (de)multiplexers interconnected by a 2-km OAM fiber that supports OAM modes. Similarly, the OAM mode (de)multiplexers are packaged first, as shown in Fig. 5(a). The experimental setup for chip–fiber–chip optical interconnects is shown in Fig. 5(b), which is similar to the setup in Fig. 4(b). The difference is that the multiplexed OAM modes are transmitted through an additional 2-km-long OAM fiber. In addition, the transmitted laser is modulated with a 20 Gbit/s quadrature phase-shift keying (QPSK) signal. At the receiver side, the output optical signals are amplified and then a coherent receiver followed by a local oscillator is used to analyze QPSK signals for the performance evaluation. Figure 5(c) shows the measured intensity profiles of the generated OAM_{-1} mode, OAM_{+1} mode, and their multiplexing after propagating through the OAM fiber. The measured crosstalk matrix for two inputs and two outputs is plotted in Fig. 5(d), which is < -10.1 dB. The measured BER curves for OAM multiplexing transmission are plotted in Fig. 5(e). Compared to the back-to-back case, the measured OSNR penalties at a BER of the 7% overhead HD-FEC threshold (3.8×10^{-3}) for multiplexing transmission of OAM_{-1} and OAM_{+1} are less than 4.6 and 5.7 dB, respectively. The insets in Fig. 5(e) are their typical constellations.

Fig. 4 (a) Middle, photo of the packaged on-chip OAM mode multiplexer and demultiplexer. Left, zoom-in view of the OAM mode multiplexer. Right, zoom-in view of the OAM mode demultiplexer. (b) Experimental setup for chip–chip optical interconnects with OAM modes. PC, polarization controller; EDFA, erbium-doped fiber amplifier; AWG, arbitrary waveform generator; OC, optical coupler; SMF, single-mode fiber; and VOA, variable optical attenuator. (c) Measured crosstalk matrix. (d) Measured BER performance and constellations.

3 Discussion

In summary, we propose and demonstrate a 3D photonic chip platform for versatile spatial mode optical interconnects. Two kinds of 3D photonic chips based on the trench waveguides are designed and fabricated for manipulating the OAM modes, including the OAM mode generation, (de)multiplexing, and exchange. The OAM spectra of the generated OAM modes output from the on-chip multiplexers are analyzed, showing a high mode purity >92%. We also demonstrate chip–chip and chip–fiber–chip optical interconnects with OAM modes using the fabricated 3D photonic chips. OAM modes multiplexing transmission carrying 8-QAM and QPSK signals are successfully demonstrated in the experiment with favorable performance.

Two OAM mode channels are employed in the experiment. There are several potential approaches that might be considered to further increase the number of mode channels. Firstly, reducing the waveguide size and rearranging them in a proper way may provide extra space for more mode channels. Secondly, a photonic lantern structure using special geometrical arrangement might be used for a large number of spatial modes,[41] and OAM modes could be obtained by using a complex trench waveguide structure. Thirdly, a free propagation region employing a Rowland circle might be used, and circular patterned apertures of 3D structures could sample and retrieve spatially overlapped multiple OAM modes.[32]

In the designed and fabricated 3D photonic chip, the bending radii of the bend waveguides are large enough (over 30 mm radius) with negligible bending loss. The propagation loss of single-mode waveguides is about 1 dB/cm. The extra loss caused by the beam splitting and combining is about 0.5 dB. The propagation loss of the trench waveguide is about
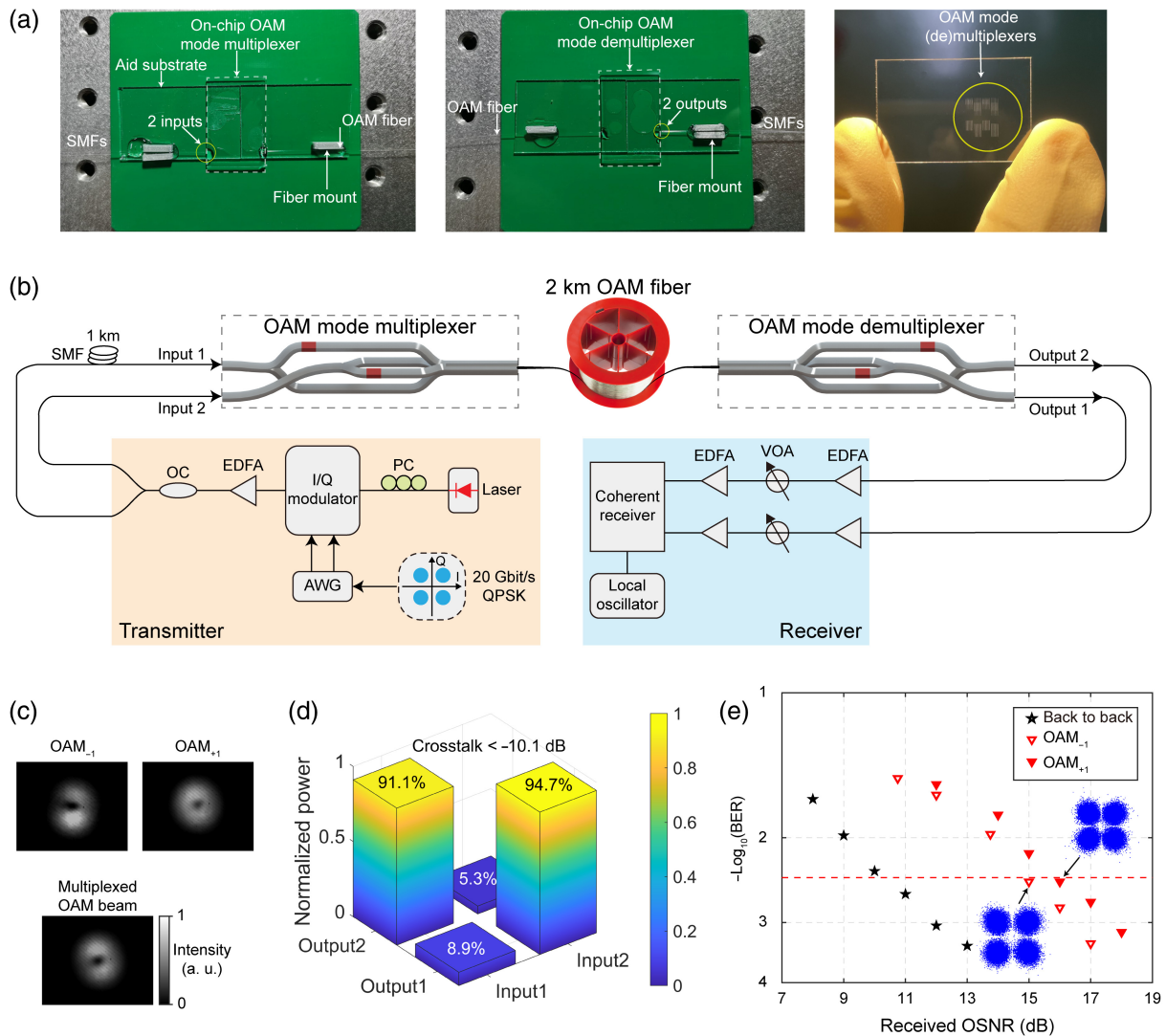
Fig. 5 (a) Photos of the packaged on-chip OAM mode multiplexer (left), OAM mode demultiplexer (middle), and unpackaged OAM mode (de)multiplexers (right) in the silica substrate. (b) Experimental setup for chip–fiber–chip optical interconnects with OAM modes. (c) Measured intensity profiles of OAM modes after propagating through the 2-km OAM fiber. (d) Measured crosstalk matrix. (e) Measured BER performance and constellations.

1.5 dB/cm. The coupling loss between the waveguide and fiber after packaging is about 1 dB/facet. The overall insertion loss of the OAM mode multiplexer is less than 5 dB. With future improvement, the propagation loss and extra loss might be reduced by optimizing the structure design and fabrication parameters. Moreover, the coupling loss might be reduced by matching the mode fields between the 3D photonic chip and fiber.

This work demonstrates a compact, multi-functional and flexible platform for tailoring the spatial structure of lightwaves and enabling chip-assisted spatial mode optical interconnects. The 3D photonic chips fabricated by the FSLW technique may find more and more exciting applications with spatial modes.

4 Appendix: Methods

4.1 3D FSLW Technique

The 3D FSLW technique is based on the laser-induced refractive index change in transparent materials. When a femtosecond

laser beam is ultrafocused inside the glass, nonlinear absorption occurs. Under the proper conditions (the pulse duration, pulse energy, and focusing numerical aperture), it will produce a localized refractive index change in the focal volume, which can reach the submicrometer scale.[42]

The setup for FSLW is depicted in Fig. 1(c). A well-polished silica substrate is mounted on the 2D stages (Aerotech), linearly moving along the x and z directions. A femtosecond laser beam reflected by a dichroic mirror propagates through an objective. The objective translating along the y direction controls the depth of the foci in the substrate during fabrication. In addition, an LED illumination propagates through a mirror, beam splitter, dichroic mirror, objective, and lightens the fabricated sample. The sample image is then reflected through the objective, dichroic mirror, beam splitter, and finally captured by a CCD. In this way, we can achieve real-time observation of fabrication. According to the tracks we program, arbitrary structures can be processed.

A femtosecond laser (PHAROS, 200 kHz repetition rate, 515 nm wavelength, and 340 fs pulse width) is focused by a 0.42 NA objective (Mitutoyo long working distance objective) at 0.2 mm below the surface of silica. The cross section of foci perpendicular to the scanning direction (z direction) is elliptical. Therefore, a mechanical slit (along the z direction) is mounted before the objective.[43,44] By adjusting the width of the slit, the Gaussian beam becomes elliptical with an ellipticity of 0.19 (defined by the ratio of the major axis and minor axis). The desired foci with a symmetric cross section can be produced. In the experiment, the pulse energy before the objective with a slit is 355 nJ. The multiscan technique is used with a scanning speed of 10 mm/s. The scanning spacing is 1.0 μm in the x direction and 0.679 μm in the y direction (considering the refractive index). The refractive index contrast is estimated to be about 3×10^{-3} to 5×10^{-3}. Additionally, the birefringence is estimated to be lower than 1×10^{-5}.

4.2 Phase Retrieving and Mode Purity Calculation

We use the off-axis digital holography technology[45,46] to reconstruct the wavefront of generated OAM beams for mode purity characterization. Off-axis digital holography allows a single-exposure acquisition of a beam wavefront by introducing a slight angle between the generated OAM beam and reference beam as they interfere at the digital camera plane. An off-axis hologram containing linear interference fringes is recorded in the experiment. We utilize a two-dimensional Fourier transform to separate the autocorrelation terms and cross-correlation terms of these linear interference fringes in the spatial-frequency domain. Since the cross-correlation terms act as a carrier for the wavefront of the OAM beam, one can retrieve the wavefront of the OAM beam by applying inverse Fourier transform to separated cross-correlation terms. Then the mode purity of the generated OAM beam can be calculated as the normalized power weight coefficient[47] using

$$|C_l| = \left| \iint \exp(i\varphi(x,y)) E_l^*(x,y) \mathrm{d}x\,\mathrm{d}y \right|^2, \qquad (2)$$

where $\varphi(x,y)$ is the measured wavefront of the generated OAM beam and $E_l(x,y)$ corresponds to the phase distribution of the conventional lth OAM beam, with the center overlapping with the generated beam. For example, to calculate the mode purity of an OAM beam with a topological charge of $+1$, $E_l(x,y)$ should be $\exp(+i\theta)$, where θ is the azimuthal angle.

References

1. D. M. Spirit, A. D. Ellis, and P. E. Barnsley, "Optical time division multiplexing: systems and networks," *IEEE Commun. Mag.* **32**(12), 56–62 (1994).
2. M. A. Khalighi, H. Akhouayri, and S. Hranilovic, "Silicon-photomultiplier-based underwater wireless optical communication using pulse-amplitude modulation," *IEEE J. Ocean Eng.* **45**(4), 1611–1621 (2020).
3. L. Tao et al. "Experimental demonstration of 10 Gb/s multi-level carrier-less amplitude and phase modulation for short range optical communication systems," *Opt. Express* **21**(5), 6459–6465 (2013).
4. X.-H. Huang et al., "WDM free-space optical communication system of high-speed hybrid signals," *IEEE Photonics J.* **10**, 7204207 (2018).
5. P. Chvojka et al., "Visible light communications: increasing data rates with polarization division multiplexing," *Opt. Lett.* **45**(11), 2977–2980 (2020).
6. D. J. Richardson, "Filling the light pipe," *Science* **330**(6002), 327–328 (2010).
7. Y. Weng, X. He, and Z. Pan, "Space division multiplexing optical communication using few-mode fibers," *Opt. Fiber Technol.* **36**, 155–180 (2017).
8. T. Mizuno and Y. Miyamoto, "High-capacity dense space division multiplexing transmission," *Opt. Fiber Technol.* **35**, 108–117 (2017).
9. A. Trichili et al., "Communicating using spatial mode multiplexing: potentials, challenges, and perspectives," *IEEE Commun. Surv. Tutor.* **21**(4), 3175–3203 (2019).
10. G. Labroille et al., "Mode selective 10-mode multiplexer based on multi-plane light conversion," in *Opt. Fiber Commun. Conf.*, OSA, Anaheim, California, p. Th3E.5 (2016).
11. S. Bade et al., "Fabrication and characterization of a mode-selective 45-mode spatial multiplexer based on multi-plane light conversion," in *Opt. Fiber Commun. Conf.*, OSA, San Diego, California, p. Th4B.3 (2018).
12. C. Koebele et al., "Two mode transmission at 2×100 Gb/s, over 40 km-long prototype few-mode fiber, using LCOS-based programmable mode multiplexer and demultiplexer," *Opt. Express* **19**(17), 16593–16600 (2011).
13. E. Otte, K. Tekce, and C. Denz, "Spatial multiplexing for tailored fully-structured light," *J. Opt.* **20**(10), 105606 (2018).
14. G. Kurczveil et al., "On-chip hybrid silicon quantum dot comb laser with 14 error-free channels," in *IEEE Int. Semicond. Laser Conf. (ISLC)*, IEEE, Santa Fe, NM, pp. 1–2 (2018).
15. Q. Bao et al., "On-chip single-mode CdS nanowire laser," *Light Sci. Appl.* **9**(1), 42 (2020).
16. K. Shtyrkova et al., "Integrated CMOS-compatible Q-switched mode-locked lasers at 1900 nm with an on-chip artificial saturable absorber," *Opt. Express* **27**(3), 3542–3556 (2019).
17. K. P. Nagarjun et al., "Generation of tunable, high repetition rate optical frequency combs using on-chip silicon modulators," *Opt. Express* **26**(8), 10744–10753 (2018).
18. A. Samani et al., "Silicon photonic Mach–Zehnder modulator architectures for on chip PAM-4 signal generation," *J. Light Technol.* **37**(13), 2989–2999 (2019).
19. Y. Zhang et al., "On-chip silicon photonic 2×2 mode- and polarization-selective switch with low inter-modal crosstalk," *Photonics Res.* **5**(5), 521–526 (2017).

20. L. Yang et al., "General architectures for on-chip optical space and mode switching," *Optica* **5**(2), 180–187 (2018).

21. X. Nie et al., "High extinction ratio on-chip pump-rejection filter based on cascaded grating-assisted contra-directional couplers in silicon nitride rib waveguides," *Opt. Lett.* **44**(9), 2310–2313 (2019).

22. W. Zhang and J. Yao, "On-chip silicon photonic integrated frequency-tunable bandpass microwave photonic filter," *Opt. Lett.* **43**(15), 3622–3625 (2018).

23. H. D. T. Linh et al., "Arbitrary TE$_0$/TE$_1$/TE$_2$/TE$_3$ mode converter using 1 × 4 Y-junction and 4 × 4 MMI couplers," *IEEE J. Sel. Top Quantum Electron.* **26**(2), 8300708 (2020).

24. Y. Meng et al., "Versatile on-chip light coupling and (de)multiplexing from arbitrary polarizations to controlled waveguide modes using an integrated dielectric metasurface," *Photonics Res.* **8**(4), 564–576 (2020).

25. X. Yu et al., "Monolithically integrated self-rolled-up microtube-based vertical coupler for three-dimensional photonic integration," *Appl. Phys. Lett.* **107**(3), 031102 (2015).

26. N. Nishiyama et al., "Si-photonics-based layer-to-layer coupler toward 3D optical interconnection," *IEICE Trans. Electron.* **E101.C**(7), 501–508 (2018).

27. M. Pospiech et al., "Single-sweep laser writing of 3D-waveguide devices," *Opt. Express* **18**(7), 6994–7001 (2010).

28. S. Gross et al., "Three-dimensional ultra-broadband integrated tapered mode multiplexers: three-dimensional ultra-broadband integrated tapered mode multiplexers," *Laser Photonics Rev.* **8**(5), L81–L85 (2014).

29. R. R. Thomson et al., "Ultrafast laser inscription of an integrated photonic lantern," *Opt. Express* **19**(6), 5698–5705 (2011).

30. H. Chen et al., "Design constraints of photonic-lantern spatial multiplexer based on laser-inscribed 3-D waveguide technology," *J. Light Technol.* **33**(6), 1147–1154 (2015).

31. G. Douglass et al., "Femtosecond laser written arrayed waveguide gratings with integrated photonic lanterns," *Opt. Express* **26**(2), 1497–1505 (2018).

32. B. Guan et al., "Free-space coherent optical communication with orbital angular, momentum multiplexing/demultiplexing using a hybrid 3D photonic integrated circuit," *Opt. Express* **22**(1), 145–156 (2014).

33. P. Mitchell et al., "57 channel (19×3) spatial multiplexer fabricated using direct laser inscription," in *Opt. Fiber Commun. Conf.*, OSA, San Francisco, California, p. M3K.5 (2014).

34. R. G. H. van Uden et al., "Ultra-high-density spatial division multiplexing with a few-mode multicore fibre," *Nat. Photonics* **8**(11), 865–870 (2014).

35. S. Gross et al., "Ultrafast laser-written sub-components for space division multiplexing," in *Opt. Fiber Commun. Conf.*, OSA, San Diego, California, p. W1A.1 (2020).

36. S. Ramachandran and P. Kristensen, "Optical vortices in fiber," *Nanophotonics* **2**(5–6), 455–474 (2013).

37. A. E. Willner et al., "Optical communications using orbital angular momentum beams," *Adv. Opt. Photonics* **7**(1), 66–106 (2015).

38. L. Zhu and J. Wang, "A review of multiple optical vortices generation: methods and applications," *Front. Optoelectron.* **12**(1), 52–68 (2019).

39. X. Wang et al., "Recent advances on optical vortex generation," *Nanophotonics* **7**(9), 1533–1556 (2018).

40. R. Chen et al., "Orbital angular momentum waves: generation, detection and emerging applications," *IEEE Commun. Surv. Tutor.* **22**(2), 840–868 (2020).

41. A. M. Velázquez-Benítez et al., "Scaling photonic lanterns for space-division multiplexing," *Sci. Rep.* **8**(1), 8897 (2018).

42. E. Mazur, "Femtosecond laser micromachining in transparent materials," in *Adv. Photonics Renew. Energy*, OSA, Karlsruhe, Germany, p. BWB4 (2010).

43. M. Ams et al., "Slit beam shaping method for femtosecond laser direct-write fabrication of symmetric waveguides in bulk glasses," *Opt. Express* **13**(15), 5676–5681 (2005).

44. Y. Cheng et al., "Control of the cross-sectional shape of a hollow microchannel embedded in photostructurable glass by use of a femtosecond laser," *Opt. Lett.* **28**(1), 55–57 (2003).

45. N. T. Shaked et al., "Off-axis digital holographic multiplexing for rapid wavefront acquisition and processing," *Adv. Opt. Photonics* **12**(3), 556–611 (2020).

46. M. Mazur et al., "Characterization of long multi-mode fiber links using digital holography," in *Opt. Fiber Commun. Conf.*, OSA, San Diego, California, p. W4C.5 (2019).

47. G. Molina-Terriza, J. P. Torres, and L. Torner, "Management of the angular momentum of light: preparation of photons in multidimensional vector states of angular momentum," *Phys. Rev. Lett.* **88**(1), 013601 (2001).

Jian Wang received his PhD in physical electronics from Wuhan National Laboratory for Optoelectronics, Huazhong University of Science and Technology, China, in 2008. He worked as a postdoctoral research associate in Optical Communications Laboratory at the University of Southern California, United States, from 2009 to 2011. Currently, he is working as a professor at Wuhan National Laboratory for Optoelectronics, Huazhong University of Science and Technology, China. He is vice director of Wuhan National Laboratory for Optoelectronics, Huazhong University of Science and Technology, China. He was elected as an OPTICA fellow (formerly OSA fellow) in 2020 and an SPIE fellow in 2022. He leads the Multi-dimensional Photonics Laboratory. His research interests include optical communications, optical signal processing, silicon photonics, photonic integration, orbital angular momentum, and structured light.

Biographies of the other authors are not available.